Article

Air Quality Monitoring for Preventive Conservation of the Built Heritage Deteriorated by Salt Crystallization

David Benavente [1,*], **Concepción Pla** [2], **Sara Gil-Oncina** [1], **Maria Candela Ruiz** [1], **Idael Francisco Blanco-Quintero** [1], **Jose Antonio Huesca-Tortosa** [3], **Yolanda Spairani-Berrio** [3] and **Sergio Sanchez-Moral** [4]

1   Department of Environmental and Earth Sciences, University of Alicante, 03690 San Vicente del Raspeig, Spain
2   Department of Civil Engineering, University of Alicante, 03690 San Vicente del Raspeig, Spain
3   Department of Architectural Constructions, University of Alicante, 03690 San Vicente del Raspeig, Spain
4   Department of Geology, National Museum of Natural Sciences (MNCN-CSIC), 28006 Madrid, Spain
*   Correspondence: david.benavente@ua.es

Abstract: The Santo Domingo Diocesan School (Orihuela, SE Spain) is a singular case study that relates air quality monitoring and stone conservation. The monument suffers severe damage due to salt crystallization by rising damp, which is related to the indoor environment dynamics, high groundwater salt content, and microstructure, the building's porous stone (biocalcarenite). Results revealed that ^{222}Rn concentration in indoor air is low due to the building's high ventilation rate, despite the medium-low geogenic radon potential in the area. Wavelets analysis showed that ventilation is caused by outdoor and indoor temperature variations and directly affects the ^{222}Rn and CO_2 dynamics inside the church. CO_2, as well as relative humidity (RH), presented periodicities with intermediate frequencies (5–8 days) related to visits. These RH and temperature (T) variations intensified the salt damage by increasing the frequency of dissolution-crystallization cycles. The mineralogical characterization and geochemical calculations concluded that chlorides (halite and sylvite), sulfates (thenardite, epsomite, hexahydrite and aphthitalite) and nitrates (niter) present from dissolution forms to whiskers and hopper-type morphologies. This indicates high saturation values and, therefore, higher crystallization pressure values within the porous media of the biocalcarenite. On the contrary, the near-equilibrium crystal shape and incongruent precipitation reaction for humberstonite suggest a lower alteration for this salt on the building stone.

Keywords: radon; salt weathering; geochemical modelling; wavelets; geogenic radon potential

1. Introduction

The concentration of indoor gases in both monuments and modern buildings can be significant, and they can impact not only their conservation but also public health and security.

Radon and carbon dioxide are two significant contaminant gases regulated by legislation in built environments. The isotope ^{222}Rn of radon is a radioactive noble gas that accumulates in the indoor air of insufficiently ventilated buildings, and it is the second most common cause of lung cancer. There are different indoor ^{222}Rn sources. The most important origin is the soil beneath the building, especially when the building is in contact with the ground. Radon can also be released into the air from construction and building materials, as well as from tap water obtained from groundwater. Carbon dioxide (CO_2) is a metabolic product, also called bioeffluent [1]. It is not considered harmful at levels usually found in buildings (600–800 ppm). Concentrations above 1000 ppm can lead to decreased attention and reduced productivity. Only prolonged exposure to critical CO_2 concentrations (6000 to 30,000 ppm) lead to increased breathing frequency, headache, nausea, vomiting, loss of consciousness, and even death [2].

However, CO_2 and ^{222}Rn monitoring has advantageous applications as indicator of indoor ventilation and air quality. Both tracer gases are used to understand ventilation patterns in different fields, including the built environment [1], caves (e.g., [3]) and different confined atmospheres as underground galleries, tunnels or mines (e.g., [4–8]). In these hypogean and underground environments, CO_2 and ^{222}Rn follow the same pattern, although they come from different sources. Monuments and hypogean constructions do not usually have ventilation systems. Particularly, CO_2 is a common indicator of room ventilation and a well-established measure of indoor air quality used, for example, for preventing the spread of the Coronavirus (SARS-CoV-2) disease (COVID-19) in workplaces [9].

In monuments, the indoor environment thermo-hygrometric conditions are fundamental for its conservation. The indoor environment is closely related to ventilation and is always more stable than the outdoor conditions as it fluctuates less and slower [10,11]. Rising damp, roof infiltrations and condensed water contribute to increase RH inside the building and their fluctuations are linked with indoor ventilation. Thus, the preventive conservation of the indoor environments in monumental buildings necessarily involves the monitoring of indoor air and characterization of ventilation patterns to guarantee adequate ambient conditions that might avoid potential damages in the indoor atmosphere [12].

The control of indoor parameters, especially RH and T, constitutes a key role in long-term building preservation [10] because the variations in thermo-hygrometric conditions and the presence of capillary pores enhance the amount of liquid water within the building elements. These elements include building materials (such as stone ashlars, clay-based materials, stuccos) and the unique art pieces they enclose (sculptures, paintings, frescoes). In this context, partial water saturation of materials offers excellent conditions for deterioration: salt crystallization, microbial degradation, reduction of their mechanical strength, chemical weathering enhanced by the presence of CO_2, etc. (e.g., [10,13–17]). Particularly, salt weathering is an important damaging agent for buildings, considered one of the most common reasons porous building materials are deteriorated as it is found in most of the built heritage.

Salt weathering of monuments occurs mostly through crystallization-dissolution cycles. These are phase changes developed under precise thermo-hygrometric conditions that depend on the thermodynamic properties of salts. Salt crystallization by rising damp in porous building materials, such as stones and mortars, occurs by the capillary transport from water table levels. On a wall, salts precipitated and crystallized at different heights in sequence according to their solubility and air temperature and relative humidity (e.g., [18–20]). Environmental monitoring can thus be proposed to minimize the damage and, at the same time, maintain healthy environmental conditions. This preventive conservation strategy must consider the nature of salts and the petrophysical properties of building materials since it is well known that salt deterioration problems might be managed through a combined process of sampling and analysis, condition assessment and environmental monitoring [21].

In this study, we investigate the indoor environment and the conservation of indoor building elements of Santo Domingo School (Orihuela, Spain). We pay special attention to the ^{222}Rn concentration in the air inside as well as in the surrounding soil and groundwater, because the geogenic radon potential in the area can be significant. ^{222}Rn and CO_2 are monitored to analyze the air dynamics and ventilation patterns from a stone conservation perspective. The monument presents intensive damage due to salt crystallization by rising damp, being the salt mineralogy, activity and distribution in the masonry linked with indoor ventilation and the nature of the groundwater placed below. Finally, we evaluate the impact of the visitors on the indoor environment and its effect on indoor salt crystallization.

2. Materials and Methods

2.1. Site and Geological Setting

The Santo Domingo Diocesan School of Orihuela is a large building, with over 21,000 m^2, catalogued as a monument of cultural interest. It was designed in 1552 by

Jerónimo Quijano, a well-known Spanish Renaissance architect, and built between the 16th and 18th centuries. The monument consists of a church (Figure 1C), a sacristy, two cloisters, a refectory, and numerous classrooms in Renaissance and Baroque styles. The building also has a 27×29 m^2 cloister with a water well (Figure 1D). The Santo Domingo School is suffering rapid and severe damage due to salt crystallization by rising damp. The water table level is close to the monument foundations and, especially after heavy rainfall, it may reach the building pavement. To minimize rising damp, some parts of the monument (particularly in the church) underwent interventions (2003–2004) consisting of the construction of air chambers under the pavement.

The prevalent climate in the area is defined as a hot semi-arid desert (Bsh climate type, Köppen–Geiger Classification [22,23]), characterized by a dry climate. For the study period (May–December 2021), outdoor conditions were defined by mean values of temperature and relative humidity of 21.4 °C and 70.0%, respectively. For this period, the total rainfall in the study area was 221 mm.

From a geological point of view, the Orihuela city is in the Western sector of the Vega Baja del Segura river basin, close to the Orihuela Range (Figure 1A). Both the basin basement and the Orihuela Range are part of the Alpujárrides Complex (Internal Betic Zone), and they are formed by low-grade metamorphic rocks, mainly Triassic metacarbonates and, to a lesser extent, phyllites and quartzites [24,25]. The carbonate rocks are intruded by mantle-derived magma crystallized near the surface, producing diabase and gabbroic rocks known as ophites. The intrusion is estimated to occur during the Late Triassic to Middle-Late Jurassic (associated with the Pangea break-off), and the metamorphic overprint is related to the Alpine Orogeny during the Eocene to Miocene. The Bajo del Segura basin is filled with Neogene-Quaternary sediments. The Santo Domingo School is located at the base of the mountain, just 50 m south from the metacarbonates and 500 m from the gabbroic rocks (Figure 1A). The basement of the building is formed by metacarbonates, located at a depth of 10 m, and covered by marls, silty and clayey materials, with the first two meters showing a certain degree of anthropic transformation.

The water table level affects the monument foundations. This region is part of the so-called "Guadalentín-Segura Quaternary Aquifer System" [26]. This system consists of two units: a surface unit (unconfined aquifer) and a deeper unit (confined aquifer). The upper unit, formed by quaternary deposits of the Segura River (sands, gravels, clay, and marls), has a water table found around two meters below the surface. The lower formation appears at ca. 70 m depth, it is separated by a clay level and is also formed by gravels, clays, and marls [26]. The groundwater quality, with high salt contents, is the result of both the intense agricultural activity in the region and the soluble nature of the geologic materials, including recent coastal processes. The amount of radon dissolved in groundwater depends also on climate, water residence time, and the interaction between water and U/Ra-bearing minerals. These geological features may turn the Santo Domingo School into a radon-prone area.

2.2. Soil, Water, and Indoor Radon Activity

Radon concentration in soils was measured for the soil in the cloister closest to the church (Figure 1B,D) within the Santo Domingo School, and also for the different types of soils in the surrounding areas. Soil radon measuring was performed using AlphaGUARD DF2000 (Saphymo GmbH, Frankfurt am Main, Germany). AlphaGUARD DF2000 has a pulse ionization chamber (alpha spectroscopy) with an integrated pump that allows measurement in diffusion and flow operation modes. It was used in the 1-min flow mode, with a 0.3 L/min pump flow, over a 15-min period. Its measurement range is between 2 Bq/m^3 and 2 MBq/m^3. Soil air samples were obtained by using small-diameter hollow steel probes (RADON-JOK) with a free, sharpened lower end (a lost tip). Soil air was extracted using a pump and collected into opaque 2 L-gas sampling bags. The depth reached in the cloister was about 0.9 m, whereas in the surrounding areas the depth ranged 0.5–0.7 m depending on the bedrock depth.
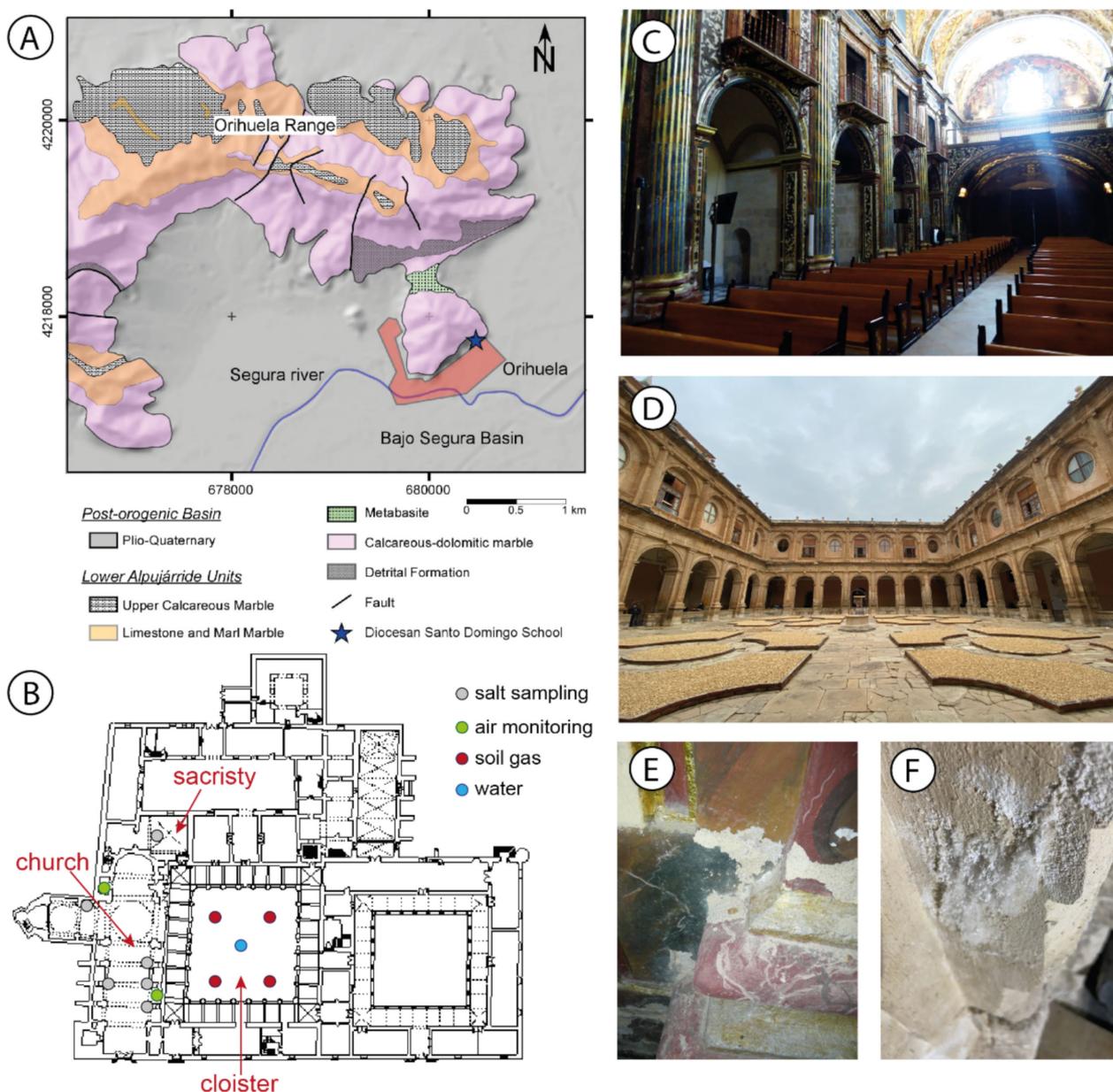
Figure 1. (**A**) Geological map of the eastern sector of Orihuela Range and Bajo Segura basin (modified after [24,25]). (**B**) Location of air monitoring and salt, soil gas and water sampling in the Diocesan Santo Domingo School. View of the (**C**) church and (**D**) cloister. Examples of deterioration patterns due to salt crystallization: (**E**) material loss (scaling and granular disintegration), and (**F**) surface modifications (efflorescences, crust and deposits).

Water was collected from the well placed in the center of the cloister (Figure 1B,D). Measurement of radon activity in water was conducted using AlphaGUARD DF2000 combined with AquaKIT (Saphymo GmbH). In a closed gas cycle, radon was expelled from the water sample by means of AlphaGUARD's electronic pump and routed through the ionization chamber where its concentration was determined. 500 mL of water were injected into the AquaKIT degassing vessel, and the gas circuit was immediately closed. Subsequently, AlphaGUARD worked on a 1-min flow mode, with a 0.5 L/min pump flow, over a 20-min period.

Indoor radon was measured using Radon Eye Plus2 (RD200P2; FTLAB Co., Ltd., Ansan, Korea). It is a real-time sensor with a pulsed ion chamber. It recorded radon air

values in the range of 1-9435 Bq/m^3 (Accuracy < ±10%), with 1 h sampling period. The continuous monitoring was calibrated using onsite measurements with AlphaGUARD.

2.3. Environment Monitoring System

Indoor environmental parameters (temperature and relative humidity) in the church were measured hourly from March to December 2021 using a HOBO MX2300 (Figure 1). In addition, from May 2021 to December 2021, CO_2 and ^{222}Rn were also measured with HOBO MX1102A and Radon Eye Plus2 devices, respectively.

Religious events in Santo Domingo School were interrupted between May and September 2021 due to different interventions in the building roofs. Consequently, the presence of people inside the building decreased considerably, which allowed the evaluation of the natural dynamic of the gases, microclimatic conditions, and the influence of people on the air quality in the building.

Daily data from outdoor environmental conditions (temperature, relative humidity, and precipitation) were acquired from AVAMET (Orihuela Centro Station), a monitoring network which offers open access to weather data.

2.4. Stone Properties and Salt Characterization

The main stones used to build the Santo Domingo School are a porous biocalcarenite and a calcodolomitic marble. The biocalcarenite is well sorted and presents fragments of red algae. It also has abundant interparticle porosity, and intraparticle porosity related to the red algae. The most abundant accessory minerals of the biocalcarenite are quartz and feldspars. The calcodolomitic marble, named Jabalina Stone, is a fine-granoblastic, heteroblastic calcitic marble with dolomite, and has xenoblastic and hypidioblastic textures. It has low porosity and its use in the building is limited to the façades portico [27]. The pore structure of the biocalcarenite was analyzed using a PoreMaster 60 GT (Quantachrome Instruments, Boynton Beach, FL, USA) mercury porosimeter, detecting pores in the pore radius interval of 0.002–200 µm.

Samples were collected from the interior of the building and analyzed using X-ray diffraction (XRD) and scanning electron microscopy (SEM). Powdered samples were characterized with a Bruker D8-Advance diffractometer with mirror Goebel using Cu Ka radiation and a setting of 40 kV and 40 mA. Data were collected and interpreted using the XPowder software package. The qualitative search matching procedure was based on the ICDD-PDF2 database. Identification of salt forms and chemical analysis of elements associated with salts was performed using a HITACHI S-3000N variable pressure electron microscope, which can analyze uncoated non-conductive samples at low beam energies. Such conditions allow a better mineral identification of the dispersive X-ray and do not compromise the integrity of analyzed hydrated salt samples. Basic microanalysis and chemical mapping were conducted using energy dispersive X-ray (SEM-EDX) using a Bruker Xash 3001 X-ray detector working at 20 kV.

Finally, the chemical composition of groundwater was determined by ion chromatography using a DIONEX DX 500. Bicarbonates were measured through neutralization titration. Electrical conductivity and pH were measured with portable conductivity and pH meters (Crison CM).

2.5. Geochemical Modelling

The geochemical reactions of dissolution-precipitation of single and double salts were modelled with PHREEQC code using 3.4.0 version [28]. PHREEQC calculates the saturation index, SI, as SI = log (IAP/K). IAP is the ion activity product and K is the equilibrium constant. The saturation index determines whether the water is saturated (equilibrium, SI = 0), undersaturated (mineral dissolution, SI < 0), or supersaturated (mineral precipitation, SI > 0) with respect to a given mineral or phase. Specific ion interaction theory (SIT) is applied to estimate single-ion activity coefficients in electrolyte solutions (sit.dat database) [29]. We selected the SIT model rather than the Pitzer model (pitzer.dat database) because the SIT

model includes the interaction coefficients for the NO_3^- species, and the ionic strength of the groundwater is relatively low (0.05 mol/kg of H_2O). The logarithm of the equilibrium constant, log K, for thenardite, mirabilite, gypsum, epsomite, hexahydrite, halite and sylvite were respectively −0.307, −1.214, −4.581, −1.851, −1.565, 1.570 and 0.900 [30], and for aphthitalite, humberstonite and niter were respectively −3.888, −7.926, −0.206 (taken from the llnl.dat database, compiled by the Lawrence Livermore National Laboratory and provided in PHREEQC version 3 [28]).

2.6. Time Series Frequency Analysis

The recorded time series of gas concentrations (CO_2 and ^{222}Rn) and thermo-hygrometric parameters (RH and T) were individually decomposed using wavelet analysis to compare pairs of signals afterwards [31,32]. Wavelet analysis allows the individualization of different frequencies within the time series, to learn the contribution of each component of the time series. The multiresolution analysis of the time series was conducted with the Environmental Wavelet Tool (EWT) [33], a Matlab-based code that also incorporates the package developed by [34]. Cross wavelet transform (XWT) and wavelet transform coherence (WTC) were calculated between pairs of the analyzed variables, aiming to identify areas with high common power in the time-frequency domain. This analysis provides the period bands in which the studied signals (CO_2 and ^{222}Rn concentration) are influenced by the thermo-hygrometric parameters (RH and T).

3. Results and Discussion

3.1. Radon Activity

^{222}Rn activity in the cloister soil is 14.62 ± 2.65 kBq/m^3, a low concentration according to Neznal et al. (2004) [35]. In the carbonate soils in the surrounding areas, ^{222}Rn soil activity ranges from 9.58 to 33.40 kBq/m^3, which can be classified as low-moderate concentration. For dry silty soil, the estimated gas permeability, kg, according to [36] methodology is 4.16×10^{-13} m^2 (pKg = −log kg = 12.38). This permeability is classified as moderate according to [35]. The classification of the radon risk is based on the geogenic radon potential (GRP) defined by [35], considering both radon soil gas concentration and gas permeability. According to this classification, soils in Santo Domingo School and surrounding areas present a low radon risk.

Indoor ^{222}Rn concentration values are very low, with a median value of 14 Bq/m^3 and a maximum value of 44 Bq/m^3 (Figure 2). The presence of visitors, in general, decreases slightly the ^{222}Rn concentration due to modifications in the ventilation pattern. These values are lower than the reference level for dwellings, as well as workplaces, established in 300 Bq/m^3 for most countries. ^{222}Rn dissolved in groundwater has a mean activity of 13.6 ± 1.0 Bq/L (Table 1), which is in concordance with typical groundwater radon concentration for aquifers in sedimentary rocks [37].

The low radon risk based on the geogenic radon potential, the concentration dissolved in water, and the high ventilation rate inside the building explain the observed indoor radon values. As a result, the adverse health effects are limited but, nevertheless, radon activity patterns can be used to evaluate ventilation and microclimate within the building, which affect its conservation.

3.2. Indoor Environment Characterization

CO_2 indoor concentration values are low (426 ± 40 ppm), below the limit value of 1000 ppm [2]. The presence of visitors, both repairing workers and assistants to religious events, increases the CO_2 concentrations up to 1124 ppm (Figure 2). After visits, CO_2 concentration rapidly reaches the average concentration. RH in the monument varies from 27.9 to 76.0%. RH fluctuations respond to the presence of visitors, and to variations in the water table position and outdoor climate conditions, both sensitive to local precipitations. Visitors produce RH short-term variations ranging from 5 to 20%. Outdoor temperature influences the indoor air temperature, with variations at both daily and annual scales (Figure 3).
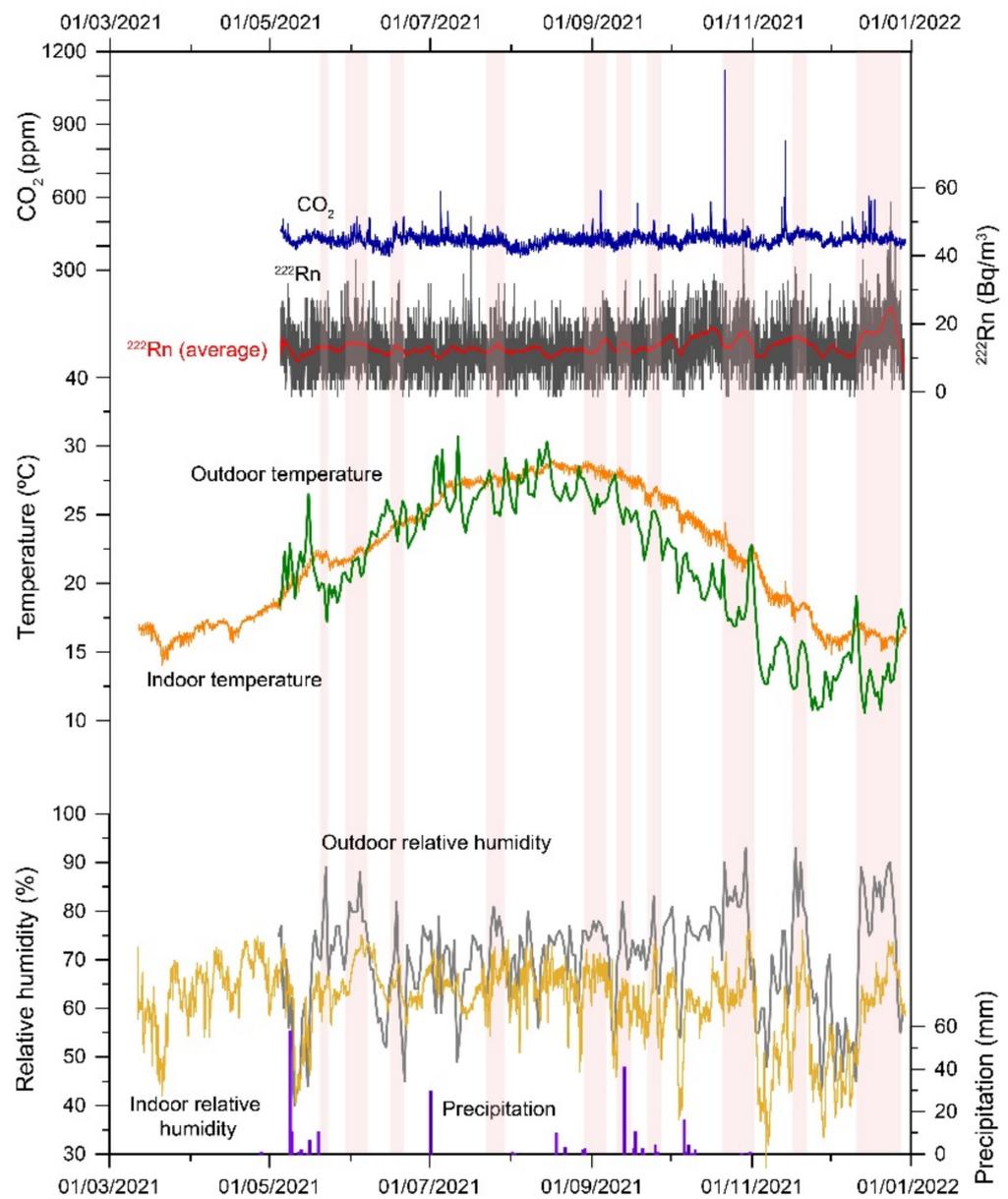
Figure 2. Temporal evolution of CO_2 (ppm) and ^{222}Rn (Bq/m^3) concentrations, outdoor (°C) and indoor (°C) temperature, outdoor (%) and indoor (%) relative humidity and precipitation (mm). Events of high outdoor humidity (>75–80%) are marked.

Table 1. Electrical conductivity (CE), pH and chemical composition of groundwater.

CE	pH	Na$^+$	K$^+$	Mg^{2+}	Ca^{2+}	Cl$^-$	SO$_4^{2-}$	HCO$_3^-$	NO$_3^-$	^{222}Rn
[mS/cm]		[ppm]	[ppm]	[ppm]	[ppm]	[ppm]	[ppm]	[ppm]	[ppm]	[Bq/L]
3.31	7.65	353.52	42.38	113.12	221.55	550.90	759.37	280.60	41.96	13.6

Individual analysis of the different signals (Figure 3) establishes the predominant periodicities for the entire evaluated period. The major contribution of gases to the time series corresponds to daily components, due to the influence of daily temperature and variations on the ventilation regime. Ventilation is caused by temperature gradients and directly affects the ^{222}Rn and CO_2 concentrations inside the church. CO_2 and ^{222}Rn frequency decomposition show a clearly defined band in the one-day periodicity. In addition, when CO_2 and ^{222}Rn are analyzed together, XWT and WTC show a high-power band in

this one-day periodicity band, highlighting that the two gases present a common behavior regulated by the ventilation regime inside the room (Figure 4).
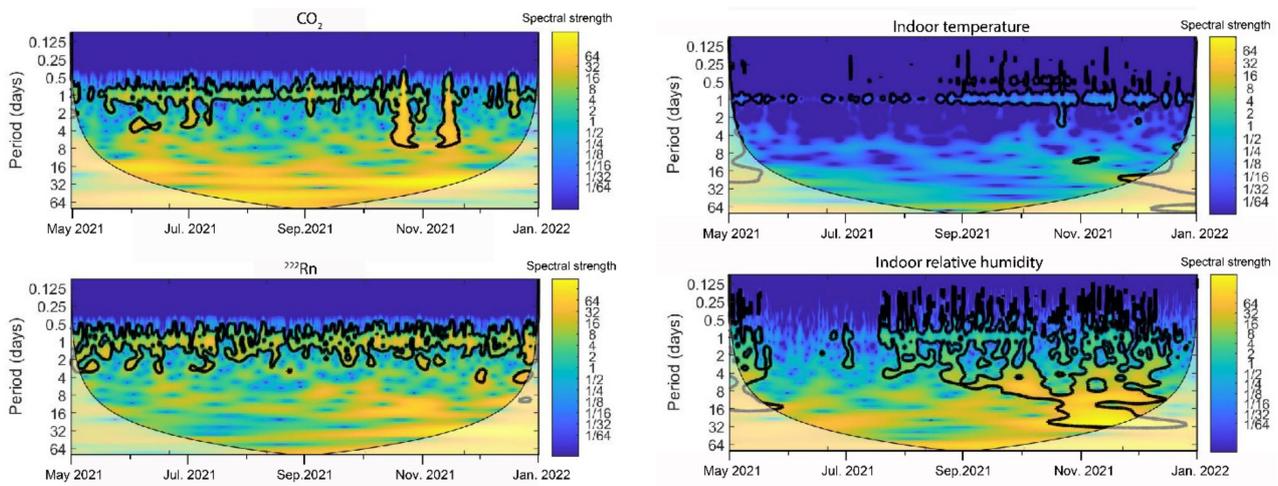

Figure 3. Decomposition of different periodicities for CO_2, ^{222}Rn, indoor temperature and indoor relative humidity.
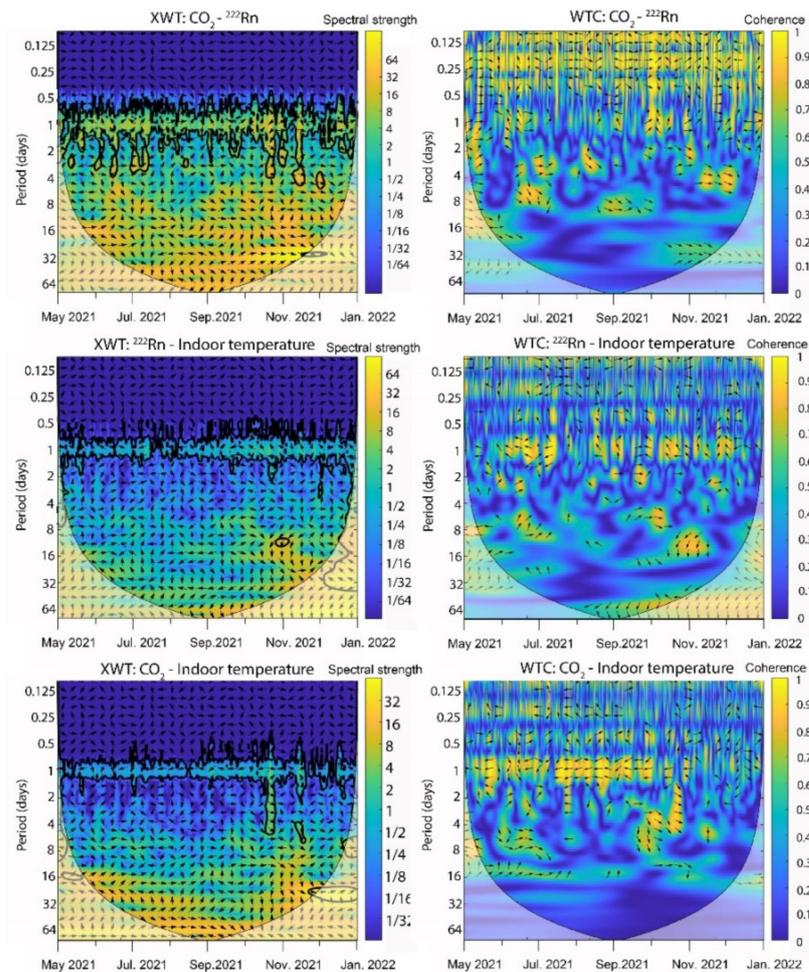

Figure 4. XWT and WTC between pair of signals: CO_2 and ^{222}Rn; ^{222}Rn and indoor temperature and CO_2 and indoor temperature. Spectral strength and coherence range from blue (weak) to yellow (strong) colors. Arrows indicate the relative phase relationship (in phase pointing right, antiphase pointing left, one signal leading the other by 90° pointing up/down). Curved lines on scalograms indicate the cone of influence where the edge effects are important.

CO_2 presents some differences with ^{222}Rn due to the presence of people in isolated events. For instance, in July, October and November the presence of visitors inside the church causes anomalous CO_2 increases that define larger periodicities for this gas in the time-period domain (Figures 2–4).

The daily periodicity of ^{222}Rn and CO_2 when they are analyzed altogether with temperature is also clearly marked within the 1-day band (Figure 4). This confirms that the changing dynamics between outdoor and indoor temperature influence the indoor environment. RH does not show a clear frequential pattern, probably because of the sensitivity to the presence of visitors. Thus, in the period of visits, RH presents more periodicities with intermediate frequencies (5–8 days) (Figure 3). This frequency band is related to the religious events conducted at the church in Santo Domingo School, which are not set every day but mainly concentrated on weekends and bank holidays. Radon concentration remains low throughout the year due to the well-ventilated atmosphere. Fluctuations in radon concentration respond to changes in weather conditions. The main variations occur in periods where the outside air relative humidity is higher than 75% (Figure 2). Effective condensation in porous materials is possible for RH values lower than 100%: it occurs when vapor pressure in the air is higher than on the rock surface, and it becomes more active due to the presence of small pores and dissolved salts [5]. For example, [15] described the effective condensation in calcarenites for RH >75%. [5] observed a similar evolution of the radon concentration in subsurface air in a hypogeal inactive-volcanic environment with RH >70%. The vapor condensation on the surface of porous building materials reduces pore size and porosity and, therefore, the passage of trace gases. Consequently, radon concentration could be used as a tracer for the condensation processes due to its high sensitivity to hygrothermal variations.

3.3. Rock Properties and Decay Pattern

The biocalcarenite of the Santo Domingo School presents high values of connected porosity (22–24%), with a main pore family in the range 0.1 to 3 μm (Figure 5). This pore structure is prone to salt weathering and capillary rise [38,39]. Thus, salt crystallization is effective in the pore interval 0.1–10 μm. Capillary movement is critical through the building porous stones because saline waters move from the foundations toward the bottom of the monument. The electrical conductivity and chemical characterization of the water well reveals the high salt content in groundwater (Table 1).
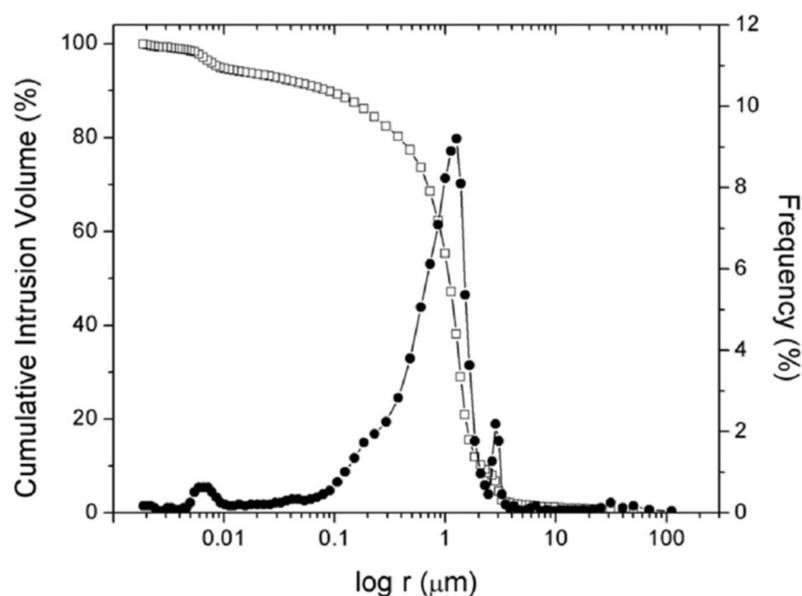

Figure 5. Cumulative intrusion volume and pore size distribution curves of studied biocalcarenite.

The alteration inside the building is concentrated in the lower portion of the walls due to rising capillary water. Two main deterioration patterns due to salt crystallization are recognized in the Santo Domingo School: surface modifications (efflorescence, crust, and deposits) and features induced by material loss (scaling, granular disintegration and alveolarization) (Figure 1E,F). These patterns are widely spread on the walls and columns. The mineralogy of salts shows both a strong vertical and horizontal variability. Different precipitation sequences are observed in the vertical profile, being the more soluble salts located at higher heights on walls and columns (Figure 1).

The analysis of the weathered material was performed using XRD and SEM; it shows the presence of mainly chlorides (halite and sylvite), sulfates (gypsum, thenardite, epsomite, hexahydrite and aphthitalite), nitrates (niter) and sulfate nitrates (humberstonite) (Figure 6). SEM images show mineral morphologies that could be related to different saturation degrees (Figure 6). Salt morphology depends on several factors such as geochemical characteristics of the saline solution, substrate where salts grow, and drying conditions. Near-equilibrium crystal shape, such as isometric shapes, denotes lower saturation degrees, whereas whiskers and hopper-type morphologies correspond to higher saturation degrees [40–42]. Results reveal that, in general, single-salt crystals have non-equilibrium shapes, as they have undergone dissolution and/or dehydration processes.
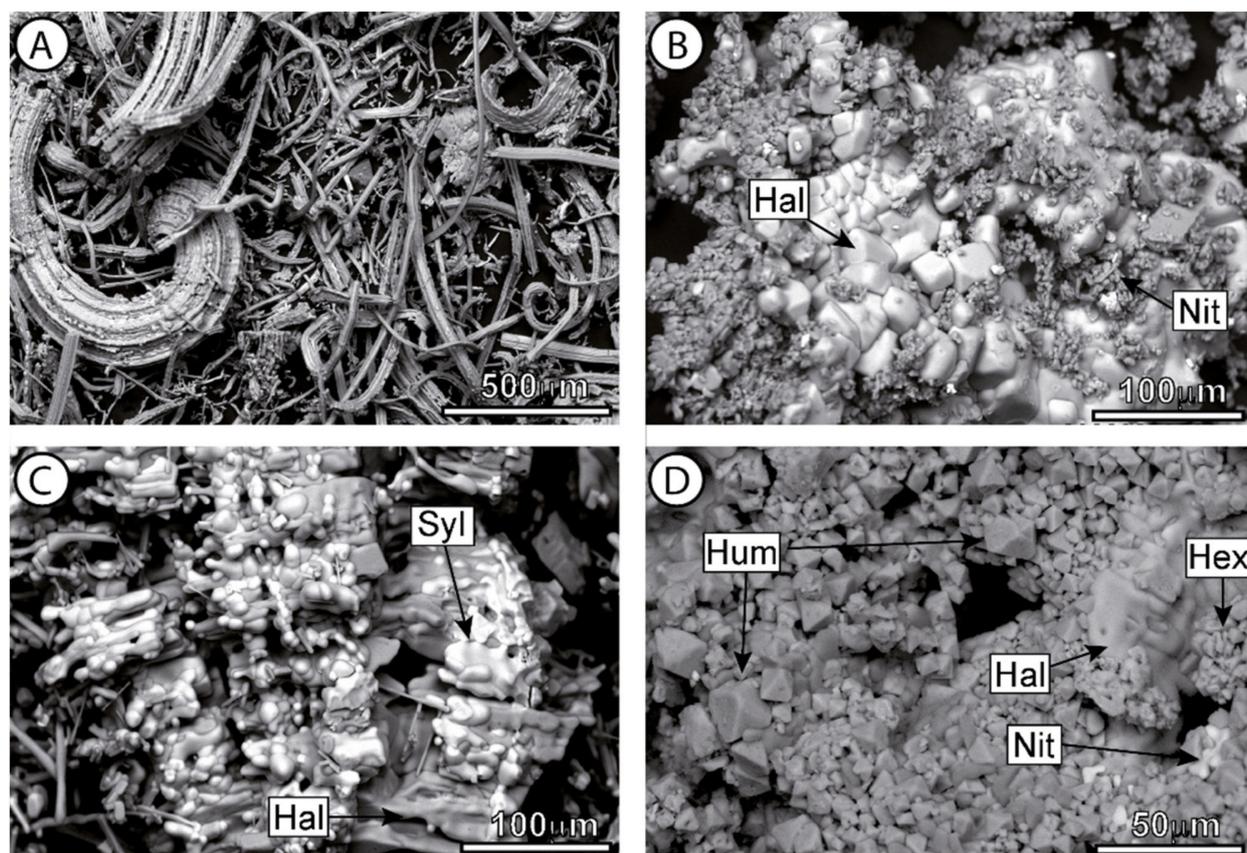

Figure 6. SEM microphotographs of salt forms from rising capillary salty waters: needle-like crystals of halite (**A**); dissolution shapes of niter (**B,D**), sylvite (**C**), and halite (**B–D**); dissolution and/or dehydration forms of hexahydrite (**B,C**); isometric shape of humberstonite (**D**). Hal: halite, Syl: sylvite; Hex: hexahydrite; Nit: niter; Hum: humberstonite.

Table 2 shows the characterized mineral phases and possible related phases. Minerals found in the XRD and SEM characterization reflect the minerals in the building, but not necessarily the mineral phases and reactions involved in their formation prior to the observed final mineral associations. For instance, the presence of thenardite may imply

the presence of mirabilite. Consequently, we cannot assert what salt in each system is responsible for the major damaging effects in each system.

Table 2. Group, mineral name, and chemical formula of salts found in the monument. Saturation index of the studied minerals for the groundwater is calculated at 25 °C.

Group	Mineral Name	Chemical Formula	Saturation Index
Sulfates	thenardite	Na_2SO_4	−6.05
	mirabilite	$Na_2SO_4 \cdot 10H_2O$	−5.14
	aphthitalite	$K_3Na(SO_4)_2$	−12.27
	gypsum	$CaSO_4 \cdot 2H_2O$	−0.68
	epsomite	$MgSO_4 \cdot 7H_2O$	−3.48
	hexahydrite	$MgSO_4 \cdot 6H_2O$	−3.76
Sulfate nitrate	humberstonite	$K_3Na_7Mg_2(SO_4)_6(NO_3)_2 \cdot 6H_2O$	−40.60
Nitrates	niter	KNO_3	−5.43
Chlorides	halite	$NaCl$	−5.36
	sylvite	KCl	−5.85

Halite clearly displays both dissolution forms of cubic and also whiskers and hopper-type morphologies (Figure 6). Halite, niter and sylvite present dissolution forms due to their high solubility and hygroscopic features. Thenardite and magnesium sulfate minerals (epsomite and hexahydrite) show dehydration forms (Figure 6B,C).

Double salts crystals, mainly humberstonite, have shapes corresponding to near-equilibrium forms, implying slow crystal growth. Figure 6D shows the humberstonite isometric shape in the analyzed samples. The saturation state of the groundwater relative to the previous set of minerals reveals that it is undersaturated (Table 1). The saturation index of single salts is higher (and close to 0) than double salts. Thus, the water evaporation within the porous materials causes, initially, the saturation and precipitation of single salts. If we consider that the water that precipitates humberstonite is obtained by niter, halite and hexahydrite dissolution, then this resulting solution is highly supersaturated (SI = 7.25) in humberstonite. According to these geochemical calculations, humberstonite precipitation is produced via an incongruent reaction rather than a congruent reaction, which explains its observed near-equilibrium forms, in concordance with the geochemical approach described by [42]. Aphthitalite is less abundant than the other observed salts. It also presents dissolution forms and is associated with niter and magnesium sulfate minerals.

The crystallization pressure that each salt causes in the pore space is determined by the supersaturation degree that each salt can reach [30]. Single salts present non-equilibrium shapes, such as whiskers and needle-like crystals (Figure 6), which indicates that salt precipitation is produced under higher supersaturation degree and, therefore, applies high crystallization pressure on the pore walls. Contrarily, double salts show a near-equilibrium crystal shape (at lower supersaturation degree) and, consequently, they produce relatively lower crystallization pressure values.

3.4. Salt Transitions by Changes in the Indoor Thermo-Hygrometric Conditions

Cycles of condensation and evaporation with subsequent cycles of dissolution-crystallization of salts that cause damage to the porous rocks are controlled by the thermo-hygrometric of the building.

Results from the analysis of the indoor environment characterization concluded that visitors influence RH and temperature. Particularly, RH variations were significant (an increase of RH = 20%, Figure 2) although the atmosphere recovers its initial conditions after visits. ^{222}Rn monitoring provides additional information not only on the ventilation pattern but also on the condensation processes, which affect the salt dissolution-crystallization dynamics. The main ^{222}Rn and indoor RH variations take place when outdoor RH >

75% (Figure 2). These indoor thermo-hygrometric variations can be critical in terms of preventive conservation when salt crystallization transitions are involved.

The precipitation of salt crystals occurs through different mechanisms closely related to changes in thermo-hygrometric conditions [30]. The chlorides and nitrates found in the monument precipitate only when the indoor relative humidity is lower than the equilibrium relative humidity of the saturated salt solution, RH_{eq}. Below this point they precipitate, and above it they absorb moisture from the air. Variations of relative humidity cause salts dissolution and re-crystallization. RH_{eq} decreases with temperature and, significantly, with the presence of other salt species.

In hydrated salts, such as magnesium and sodium sulfates, dissolution of the lower hydrated form followed by precipitation of the hydrated salt is the most aggressive weathering mechanism for these types of salts. For example, in the magnesium sulfate-water system, water, from rising damp and/or condensation, dissolves the powdered hexahydrate crystals and produces solutions highly supersaturated with epsomite. This precipitation pathway occurs by crossing the phase boundary, and it can generate enough stress to damage the stone. The critical relative humidity, RH_{Crit}, for the hexahydrate–epsomite phase transition can be defined from the equilibrium constants of hexahydrate and epsomite. In the equilibrium, RH_{Crit} is related to the water activity, a_w, and can be calculated using the equilibrium constants of the hydrated salt, K_A, and the lower hydrated form, K_B, as:

$$RH_{Crit} = a_w = (K_A/K_B)^{\frac{1}{(n_A - n_B)}},$$

where n_A and n_B are the number of water molecules of the hydrated and the lower hydrated form, respectively. Since equilibrium constants depend only on temperature, at constant pressure, the critical relative humidity is not influenced by the presence of other salt species. Thus, RH_{Crit} the critical relative humidity can be obtained using the variation of equilibrium constants with temperature (e.g., [30]).

Figure 7A plots indoor relative humidity, and the equilibrium and critical relative humidity for the anhydrous and hydrated mineral phases. The most active salt system is the magnesium sulfate, since the indoor RH and the hexahydrite-epsomite critical relative humidity cross paths in several different periods within the time series.

This salt activity is also shown in the magnesium sulfate phase diagram (Figure 7C), where thermo-hygrometric values were recorded during the monitoring period crossing the hexahydrite-epsomite phase boundary. Ref. [43] presented a revised and completed phase diagram for the MgSO$_4$ system. Figure 7C represents a simplified version of this diagram, considering the epsomite and hexahydrite transitions. We focused this study on these salts because they were detected using XRD. However, the presence of other MgSO$_4$ salts, such as pentahydrate (MgSO$_4$·5H$_2$O), starkeyite (MgSO$_4$·4H$_2$O) and kieserite (MgSO$_4$·H$_2$O), during the dissolution-precipitation processes may be likely. Below 20 °C, there is no stable phase boundary between epsomite and hexahydrite, but between epsomite and kieserite (MgSO$_4$·H$_2$O) [43], which was not detected under XRD. Moreover, the kinetics of epsomite and hexahydrite salt transitions is slow [43] and, consequently, the effectiveness of the salt weathering must be considered lower than the one predicted by the thermodynamic approach.

The sodium sulfate system is less active than the magnesium sulfate minerals. Thernadite prevails for most of the period without undergoing significant dissolution-crystallization processes (Figure 7D). Figure 7B shows that chlorides and nitrates also present minor activity, and results indicate that they will remain precipitated. This explains the extensive amounts of halite efflorescence across the inner walls. However, RH_{eq} may decrease with the presence of other ions in the solution. For highly saline waters, RH_{eq} can drop its value between 5–10% compared to the saturated salt solution in pure water [30]. Consequently, an increase in salts dissolution and re-crystallization cycles are expected compared to the estimations shown in Figure 7A,B.
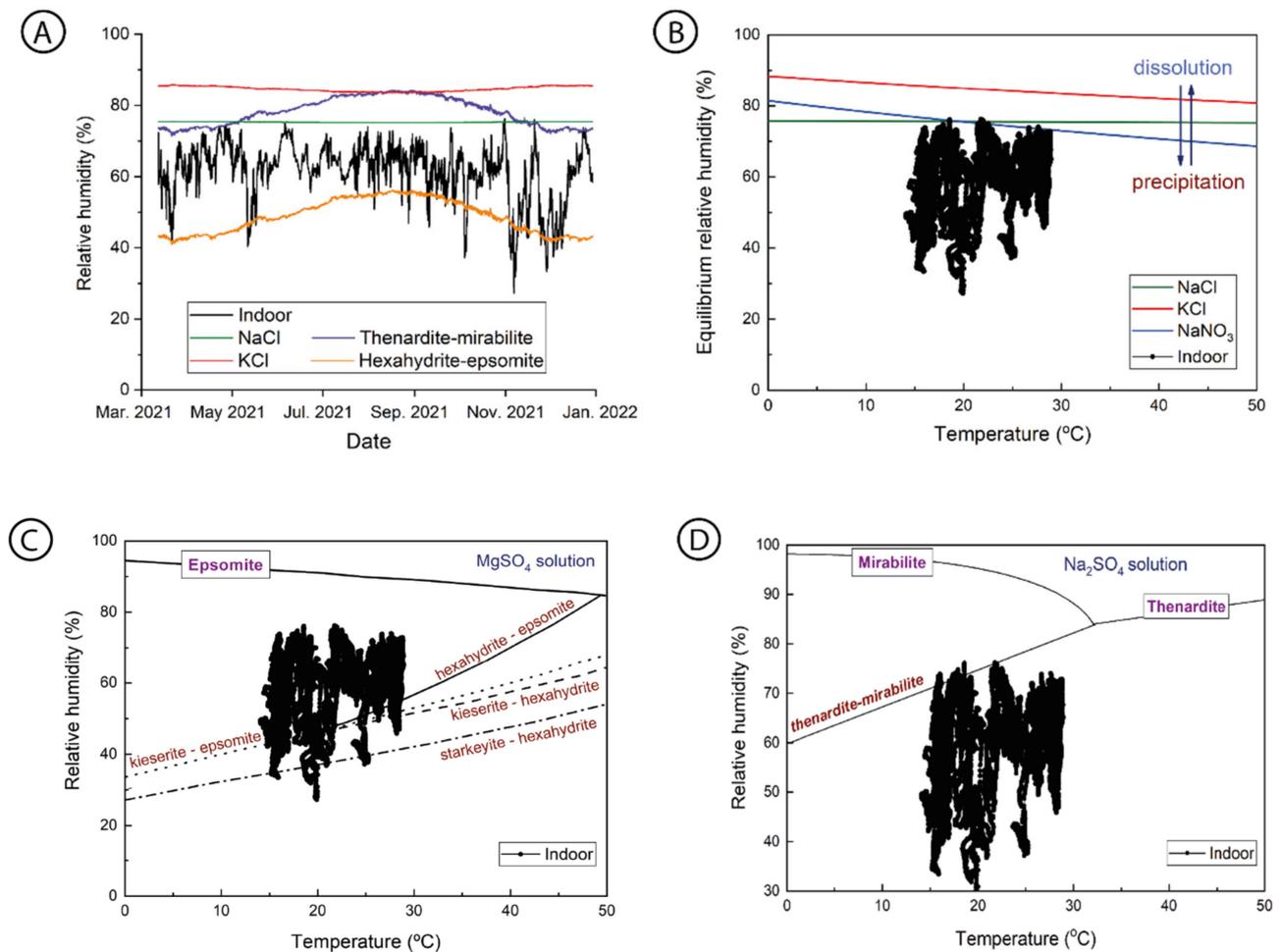
Figure 7. (**A**) Indoor relative humidity and the equilibrium and critical relative humidity for the anhydrous and hydrated mineral phases. Phase diagram of the (**B**) anhydrous salts (halite-NaCl, sylvite-KCl and niter-NaNO$_3$), (**C**) magnesium sulfate (solid line: epsomite-MgSO$_4$·7H$_2$O and hexahydrite-MgSO$_4$·6H$_2$O; dashed line: hexahydrite-MgSO$_4$·6H$_2$O and kieserite-MgSO$_4$·H$_2$O; dotted line: epsomite-MgSO$_4$·7H$_2$O and kieserite-MgSO$_4$·H$_2$O; dash dotted line: hexahydrite-MgSO$_4$·6H$_2$O and starkeyite-MgSO$_4$·4H$_2$O), (**D**) sodium sulfate (mirablite-Na$_2$SO$_4$·10H$_2$O and thenardite-Na$_2$SO$_4$).

Results also reveal that visitors modify indoor RH and temperature and may intensify the salt damage by increasing the frequency of dissolution-crystallization cycles.

Salt crystallization comprises other kinetic factors not considered in this investigation, such as salt nucleation, kinetics of the phase transitions, rate of water condensation and evaporation, and the capillary flow of groundwater from the basement. Saturation index and phase diagrams provide thermodynamic information that qualitatively evaluates the effectiveness of the salt damage. Thus, the critical supersaturation required for nucleation, the crystal growth rate (eg. [44]), and the crystallization pressure (eg. [45]) rise as the saturation index increases. Phase diagrams then also provide information on the activity of each salt system, which increases along the frequency of salt transitions [30].

4. Conclusions

In this study, we investigated the indoor environment dynamics and the relationship between air quality and stone conservation at Santo Domingo School. Despite the low-medium geogenic radon potential of the area, the ^{222}Rn concentration in the building is low. This is due to the presence of a well-ventilated air chamber in the building, which

limits the adverse health effects. CO_2 indoor concentration values are also low, close to the standard atmospheric CO_2 concentration. However, the presence of visitors, mostly during religious events, increases the CO_2 concentrations from 150 to 600 ppm.

Wavelet analysis reveals that ventilation is caused by outdoor and indoor temperature variations, and directly affects the ^{222}Rn and CO_2 concentration inside the church. CO_2, however, presents some differences with ^{222}Rn due to the presence of people in isolated events. For instance, the religious events in July, October and November caused the CO_2 larger periodicities in the time-period domain. The frequential pattern of RH is different than ^{222}Rn and CO_2 patterns due to the sensibility of RH to the presence of visitors. Thus, during the period of visits, RH presents more periodicities with intermediate frequencies (5–8 days) related to the religious events rather than daily periodicities caused by outdoor and indoor temperature variations.

The presence of visitors modifies indoor RH and temperature, and intensifies the salt damage by increasing the frequency of dissolution-crystallization cycles. The monument presents intensive damage due to salt crystallization by rising damp. Due to its pore structure, the biocalcarenite used as a building material in Santo Domingo is prone to be damaged by salt weathering and active capillary transport. Capillary movement is critical in this context because the groundwater presents a high salt content. The mineralogy and distribution follow a precipitation sequence, with the more soluble salts located at higher heights of walls and columns.

The most active salt system is the magnesium sulfate, due to the critical relative humidity of hexahydrite-epsomite intersecting the indoor RH at different periods of the time series, mostly from the beginning of the visits. The sodium sulfate system is less active than the magnesium sulfate minerals.

Chlorides and nitrates are also active due to RH_{eq} decreases with the presence of other ions in the solution. It increases the frequency in which indoor RH and RH_{eq} are crossing and, consequently, the frequency of salts dissolution and re-crystallization. Within long periods of low indoor relative humidity, these single salts mainly remain precipitated, which explains the extensive amounts of halite efflorescence across the inner walls. Halite clearly presents both dissolution forms and whiskers and hopper-type morphologies, which indicates high values of saturation. Thenardite and hexahydrite show dehydration forms that are related to the activity of dissolution-crystallization cycles. Thus, these non-equilibrium forms indicate a high supersaturation degree of the minerals, and consequently, higher crystallization pressure within the porous space of the biocalcarenite. Contrarily, humberstonite shows a near-equilibrium crystal shape (at low supersaturation degree), and it produces relatively lower damage to the porous rock.

Author Contributions: Conceptualization, D.B.; Methodology, S.G.-O., M.C.R., I.F.B.-Q., J.A.H.-T. and Y.S.-B.; Validation, C.P., S.S.-M. and D.B.; Investigation, S.G.-O., M.C.R., I.F.B.-Q., J.A.H.-T. and Y.S.-B.; Data Curation, C.P., S.G.-O. and M.C.R.; Writing—Original Draft Preparation, D.B.; Writing—Review and Editing, M.C.R., C.P. and S.S.-M.; Visualization, S.S.-M. and C.P.; Supervision, D.B.; Funding Acquisition, D.B. All authors have read and agreed to the published version of the manuscript.

References

1. Dovjak, M.; Vene, O.; Vaupotič, J. Analysis of Ventilation Efficiency as Simultaneous Control of Radon and Carbon Dioxide Levels in Indoor Air Applying Transient Modelling. *Int. J. Environ. Res. Public Health* **2022**, *19*, 2125. [CrossRef] [PubMed]
2. Küçükhüseyin, Ö. CO_2 monitoring and indoor air quality. *REHVA J.* **2021**, *1*, 45–59.
3. Pla, C.; Fernandez-Cortes, A.; Cuezva, S.; Galiana-Merino, J.J.; Cañaveras, J.C.; Sanchez-Moral, S.; Benavente, D. Insights on Climate-Driven Fluctuations of Cave ^{222}Rn and CO_2 Concentrations Using Statistical and Wavelet Analyses. *Geofluids* **2020**, *2020*, 8858295. [CrossRef]
4. Eff-Darwich, A.; Vinas, R.; Soler, V.; de la Nuez, J.; Quesada, M.L. Natural air ventilation in underground galleries as a tool to increase radon sampling volumes for geologic monitoring. *Radiat. Meas.* **2008**, *43*, 1429–1436. [CrossRef]
5. Fernández-Cortés, A.; Benavente, D.; Cuezva, S.; Cañaveras, J.C.; Alvarez-Gallego, M.; Garcia-Anton, E.; Soler, V.; Sanchez-Moral, S. Effect of water vapour condensation on the radon content in subsurface air in a hypogeal inactive-volcanic environment in Galdar Cave, Spain. *Atmos. Environ.* **2013**, *75*, 15–23. [CrossRef]
6. Wang, S.G.; Niu, X.B.; Chen, Q.; Yang, W. Radon Exhalation Patterns in A Dead-end Tunnel. In Proceedings of the 2016 International Conference on Mechatronics, Manufacturing and Materials Engineering, Hong Kong, China, 11–12 June 2016; Volume 63.
7. Skubacz, K.; Wysocka, M.; Michalik, B.; Dziurzynski, W.; Krach, A.; Krawczyk, J.; Palka, T. Modelling of radon hazards in underground mine workings. *Sci. Total. Environ.* **2019**, *695*, 133853. [CrossRef]
8. Ajayi, K.; Shahbazi, K.; Tukkaraja, P.; Katzenstein, K. Numerical investigation of the effectiveness of radon control measures in cave mines. *Int. J. Min. Sci. Technol.* **2019**, *29*, 469–475. [CrossRef]
9. REHVA (Federation of European Heating, Ventilation and Air Conditioning Associations). *REHVA COVID-19 Guidance Document How to Operate HVAC and Other Building Service Systems to Prevent the Spread of the Coronavirus (SARS-CoV-2) Disease (COVID-19) in Workplaces*; REHVA: Brussels, Belgium, 2021.
10. Camuffo, D. *Microclimate for Cultural Heritage—Conservation, Restoration and Maintenance of Indoor and Outdoor Monuments*; Elsevier: Amsterdam, The Netherlands, 2013.
11. Brimblecombe, P. Heritage climatology. In *Climate Change and Cultural Heritage*; Lefevre, R.A., Sabbioni, C., Eds.; Edipuglia: Bari, Italy, 2010; pp. 54–57.
12. Díaz-Arellano, I.; Zarzo, M.; García-Diego, F.-J.; Perles, A. A Methodology for the Multi-Point Characterization of Short-Term Temperature Fluctuations in Complex Microclimates Based on the European Standard EN 15757:2010: Application to the Archaeological Museum of l'Almoina (Valencia, Spain). *Sensors* **2021**, *21*, 7754. [CrossRef]
13. West, G. Effect of suction on the strength of rock. *Q. J. Eng. Geol. Hydrogeol.* **1994**, *27*, 51–56. [CrossRef]
14. Sanchez-Moral, S.; Luque, L.; Cuezva, S.; Soler, V.; Benavente, D.; Laiz, L.; Gonzalez, J.M.; Saiz-Jimenez, C. Deterioration of building materials in Roman catacombs: The influence of visitors. *Sci. Total Environ.* **2005**, *349*, 260–276. [CrossRef]
15. Benavente, D.; Sanchez-Moral, S.; Fernandez-Cortes, A.; Canaveras, J.C.; Elez, J.; Saiz-Jimenez, C. Salt damage and microclimate in the Postumius Tomb, Roman Necropolis of Carmona, Spain. *Environ. Earth Sci.* **2011**, *63*, 1529–1543. [CrossRef]
16. Lopez-Doncel, R.; Wedekind, W.; Dohrmann, R.; Siegesmund, S. Moisture expansion associated to secondary porosity: An example of the Loseros Tuff of Guanajuato, Mexico. *Environ. Earth Sci.* **2013**, *69*, 1189–1201. [CrossRef]
17. Cañaveras, J.C.; Fernandez-Cortes, A.; Elez, J.; Cuezva, S.; Jurado, V.; Miller, A.Z.; Rogerio-Candelera, M.A.; Benavente, D.; Hernandez-Marine, M.; Saiz-Jimenez, C.; et al. The deterioration of Circular Mausoleum, Roman Necropolis of Carmona, Spain. *Sci. Total Environ.* **2015**, *518*, 65–77. [CrossRef]
18. Arnold, A. *Rising Damp and Saline Minerals, Proceedings of the 4th International Congress on the Deterioration and Preservation of Stone Objects, Louisville, KY, USA, 7–8 July 1982*; Gauri, K.L., Gwinn, J.A., Eds.; University of Louisville: Louisville, KY, USA, 1982.
19. Arnold, A.; Zehnder, K. Salt weathering on monuments. In *First International Symposium on the Conservation of Monuments in the Mediterranean Basin*; Zezza, F., Ed.; Grafo: Bari, Italy, 1990; pp. 31–58.
20. Lopez-Arce, P.; Doehne, E.; Greenshields, J.; Benavente, D.; Young, D. Treatment of rising damp and salt decay: The historic masonry buildings of Adelaide, South Australia. *Mater. Struct.* **2009**, *41*, 827–848. [CrossRef]
21. Sawdy, A.; Price, C.A. Salt damage at Cleeve Abbey, England. Part I: A comparison of theoretical predictions and practical observations. *J. Cult. Herit.* **2005**, *6*, 125–135. [CrossRef]
22. Köppen, W. Das geographische System der Klimate. In *Handbuch der Klimatologie*; Koppen, W., Geiger, R., Eds.; Gebrüder Borntraeger Verlagsbuchhandlung: Berlin, Germany, 1936; Volume I, Part C.
23. Beck, H.E.; Zimmermann, N.E.; Mcvicar, T.R.; Vergopolan, N.; Berg, A.; Wood, E.F. Data Descriptor: Present and future Köppen-Geiger climate classification maps at 1-km resolution. *Sci. Data.* **2018**, *5*, 180214. [CrossRef]
24. De Boer, A.; Egeler, C.G.; Kampschuur, W.; Montenat, C.H.; Rondeel, H.E.; Simon, O.J.; van Winkoop, A.A. *Mapa Geológico y Memoria de la Hoja Geológica nº 913 (Orihuela). Mapa Geológico de España. 1:50.000*, 1st ed.; MAGNA 2; IGME: Madrid, Spain, 1951; 40p.
25. Martín-Rojas, I.; Estévez, A.; Martín-Martín, M.; Delgado, F.; García-Tortosa, F.J. New data from Orihuela and Callosa Mountains (Betic Internal Zone, Alicante, SE Spain). Implications for the "Almágride Complex" controversy. *J. Iber. Geol.* **2007**, *33*, 311–318.
26. IGME. *Las Aguas Subterráneas en la Comunidad Valenciana. Uso, Calidad y Perspectivas de Utilización*; Instituto Geológico y Minero de España: Madrid, Spain, 1988.

27. Benavente, D.; Bernabeu, A.; Fort, R.; Martinez-Martinez, J.; Garcia-del-Cura, M.A. The decolouration of brecciated black marbles used in heritage monuments of Alicante. In *Heritage, Weathering and Conservation*; Fort, R., Alvarez de Buergo, M., Gomez-Heras, M., Vazquez-Calvo, C., Eds.; Balkema: Rotterdam, The Netherlands, 2006; pp. 205–210.

28. Parkhurst, D.L.; Appelo, C.A.J. Description of input and examples for PHREEQC version 3—A computer program for speciation, batch-reaction, one-dimensional transport, and inverse geochemical calculations. In *U.S. Geological Survey Techniques and Methods*; United States Geological Survey: Reston, VA, USA, 2013.

29. Langmuir, D. *Aqueous Environmental Geochemistry*; Prentice Hall: Sacramento, CA, USA, 1997.

30. Benavente, D.; Brimblecome, P.; Grossi, C.M. Thermodynamic calculations for the salt crystallisation damage in porous built heritage using PHREEQC. *Environ. Earth Sci.* **2015**, *74*, 2297–2313. [CrossRef]

31. Daubechies, I. *Ten Lectures on Wavelets*; Society for Industrial and Applied Mathematics: Philadelphia, PA, USA, 1992.

32. Wickerhauser, M.V. *Adapted Wavelet Analysis from Theory to Software*; A K Peters: Natick, MA, USA; CRC Press: Boca Raton, FL, USA, 1996.

33. Galiana-Merino, J.J. EnvironmentalWaveletTool: Continuous and discrete wavelet analysis and filtering for environmental time series. *Comput. Phys. Commun.* **2014**, *185*, 2758–2770. [CrossRef]

34. Grinsted, A.; Moore, J.C.; Jevrejeva, S. Application of the cross wavelet transform and wavelet coherence to geophysical time series. *Nonlinear Process. Geophys.* **2004**, *11*, 561–566. [CrossRef]

35. Benavente, D.; Valdes-Abellan, J.; Pla, C.; Sanz-Rubio, E. Estimation of soil gas permeability for assessing radon risk using Rosetta pedotransfer function based on soil texture and water content. *J. Environ. Radioact.* **2019**, *208–209*, 105992. [CrossRef] [PubMed]

36. Neznal, M.; Matolín, M.; Barnet, I.; Mikšová, J. New method for assessing the radon risk of building sites. In *Czech Geological Survey Special Papers 1*; CGS: Prague, Czech Republic, 2004; p. 47.

37. European Union Law. Commission Recommendation of 20 December 2001 on the protection of the public against exposure to radon in drinking water supplies (notified under document number C (2001) 4580). *Off. J. L* **2001**, *344*, 85–88.

38. Benavente, D. Why pore size is important in the deterioration of porous stones used in the built heritage? *Macla* **2011**, *15*, 41–42.

39. Benavente, D.; Martinez-Martinez, J.; Cueto, N.; Ordonez, S.; Garcia-del-Cura, M.A. Impact of salt and frost weathering on the physical and durability properties of travertines and carbonate tufas used as building material. *Environ. Earth Sci.* **2018**, *77*, 147. [CrossRef]

40. Rodriguez-Navarro, C.; Dohene, E. Salt weathering: Influence of evaporation rate, supersaturation and crystallisation pattern. *Earth Surf. Process. Landf.* **1999**, *24*, 191–209. [CrossRef]

41. Sunagawa, I. *Crystals: Growth, Morphology and Perfection*; Cambridge University Press: Cambridge, UK, 2005.

42. Benavente, D.; de Jongh, M.; Cañaveras, J.C. Weathering Processes and Mechanisms Caused by Capillary Waters and Pigeon Droppings on Porous Limestones. *Minerals* **2021**, *11*, 18. [CrossRef]

43. Steiger, M.; Linnow, K.; Ehrhardt, D.; Rohde, M. Decomposition reactions of magnesium sulfate hydrates and phase equilibria in the $MgSO_4$–H_2O and Na^+–Mg^{2+}–Cl^-–SO_4^{2-}–H_2O systems with implications for Mars. *Geochim. Cosmochim. Acta* **2011**, *75*, 3600–3626. [CrossRef]

44. Lasaga, A.C. *Kinetic Theory in the Earth Sciences*; Princeton University Press: Chichester, UK; Princeton, NJ, USA, 1998.

45. Correns, C.W. Growth and dissolution of crystals under linear pressure. *Disc. Faraday Soc.* **1949**, *5*, 267–271. [CrossRef]